On the stable estimation of flow geometry and wall shear stress from magnetic resonance images

OPEN ACCESS
IOP Publishing
Inverse Problems
Inverse Problems **35** (2019) 095001 (23pp)
https://doi.org/10.1088/1361-6420/ab23d5

On the stable estimation of flow geometry and wall shear stress from magnetic resonance images

H Egger and G Teschner

AG Numerik, TU Darmstadt, Dolivostraße 15, 64293 Darmstadt, Germany

E-mail: egger@mathematik.tu-darmstadt.de
and teschner@mathematik.tu-darmstadt.de

Received 24 December 2018, revised 29 March 2019
Accepted for publication 22 May 2019
Published 23 August 2019

Abstract

We consider the stable reconstruction of flow geometry and wall shear stress from measurements obtained by magnetic resonance imaging (MRI). As noted in a review article by Petersson, most approaches considered so far in the literature seem to not be satisfactory. We therefore propose a systematic reconstruction procedure that allows us to obtain stable estimates of flow geometry and wall shear stress and we are able to quantify the reconstruction errors in terms of bounds for the measurement errors under reasonable smoothness assumptions. A complete analysis of our approach is given in the framework of regularization methods. In addition, we briefly discuss the implementation of our method and we demonstrate its viability, accuracy, and regularizing properties for experimental data.

Keywords: wall shear stress estimation, magnetic resonance imaging, ill-posed problems, Tikhonov regularization, conditional stability

(Some figures may appear in colour only in the online journal)

1. Introduction

Wall shear stress has been identified to have an impact on the regulation of endothelial cells [10, 19] and therefore as one important influential factor in the development of arterial diseases such as aneurysms [23] and arteriosclerosis [4]. Due to its clinical relevance, the estimation of wall shear stress, i.e. of the normal derivative of tangential velocity components at arterial walls, has attracted significant interest in the literature; see [3, 15, 20–22, 25] and the

references therein. Unfortunately, most of the approaches utilized so far suffer at least from one of the following artifacts:

- for low data resolution wall shear stress is systematically underestimated;
- for high data resolution the estimates become increasingly unstable.

Let us briefly discuss some explanations for these problems: internal measurements are used in [20] to fit cubic polynomials to the flow profile. In the presence of logarithmic turbulent boundary layers [12], this leads to a flattened approximation of the velocity near the boundary, thus underestimating the velocity derivative and overestimating the radius of the flow region. Due to a kink of the velocity profile at the boundary, a spline interpolation in the whole domain, as proposed in [25], leads to inaccurate representation of the velocity, in particular, near the boundary, which makes the estimate of wall shear stress unreliable. These observations are amplified by the fact that noise in the velocity measurements can be expected to be particularly high close to the boundary; compare with the data in section 6 and the remarks in the appendix. Let us note that even for exact velocity data the evaluation of the wall shear stress is unstable with respect to the boundary location due to the discontinuity of the normal derivative of velocity at the boundary. These observations made the authors of [21] conclude that *even in the absence of noise and for relatively simple velocity profiles, all methods evaluated were found to be impacted by considerable errors*.

In this paper, we investigate the stable estimation of flow geometry, velocity, and wall shear stress by a problem adapted approach that overcomes the above difficulties and that allows for a rigorous stability and convergence analysis. The overall reconstruction problem will be decomposed into the following three natural steps:

(i) estimation of the flow boundary from magnetic standard resonance images of proton density (geometry identification);
(ii) reconstruction of flow velocity from phase contrast images in a function class that ensures zero velocity at the estimated flow boundary (velocity estimation);
(iii) evaluation of the normal derivative of the velocity at the boundary of the flow domain (wall shear stress computation).

Various methods for the individual subproblems are available, and we here consider one particular combination of such approaches that allows us to conduct a full convergence analysis of the overall reconstruction process under reasonable smoothness assumptions.

Let us briefly discuss and motivate our selection of methods: while standard edge detection algorithms [2] and level set methods [16] allow for a systematic image segmentation, we here utilize a parametric approach for the geometry identification problem (i) which not only allows for a full analysis in the context of Tikhonov regularization, but also provides an explicit geometry representation that is the basis for the systematic handling of the second and third subproblem. The velocity estimation problem (ii) is a denoising problem which can be tackled by standard filter methods. Here we employ a variational filter defined by Tikhonov regularization [8, 28] and explicitly incorporate no-slip boundary conditions at the reconstructed vessel wall. The incorporation of these boundary conditions is an essential step in our approach. The computation of wall-shear stress from approximations of the geometry and velocity in step (iii) amounts to numerical differentiation and evaluation of polynomials. Due to the particular choice of regularization terms in the first two subproblems, we are able to guarantee stability of this post-processing step.

The focus of the current paper is on the rigorous analysis of a specific approach for the systematic estimation of wall-shear stress from magnetic resonance measurements. For illustration of the viability of our theoretical results, we also discuss briefly the numerical

implementation and present reconstructions obtained for experimental data. In contrast to previous approaches [3, 20–22, 25], we obtain accurate and stable estimates for the wall-shear stress even for rather low data resolution which can be explained by our analysis. Let us note that, for the two dimensional setting considered in this paper, all reconstructions can be computed in seconds, while the measurement times are in the order of minutes. We therefore do not comment in detail on the efficient implementation or computation times.

The rest of the manuscript is organized as follows: for the geometry identification, we consider in section 2 a parametric formulation which leads to a nonlinear inverse problem with a non-differentiable forward operator. We prove a conditional stability estimate and derive convergence rates for Tikhonov regularization under simple smoothness assumptions on the true geometry. The resulting parametrization of the flow domain is then used in section 3 to formulate the velocity reconstruction problem on a reference domain, resulting in a linear inverse problem with additional data perturbation stemming from the inexact geometry representation. Again, a full convergence analysis of Tikhonov regularization for this problem is presented. By choosing sufficiently strong regularization terms in the first two steps, we obtain stability of the geometry and velocity reconstruction in strong norms which allows us to compute estimates for the wall-shear stress in a stable way. This is demonstrated in section 4. For ease of presentation, some technical details of the analysis are shifted to the appendix. While most of our analysis is presented for two dimensional measurements, we briefly comment in section 5 also on the natural extension of our results to three dimensions. In addition to the complete theoretical analysis of our approach, we briefly discuss in section 6 its numerical realization and demonstrate its viability by application to experimental data.

2. Geometry identification

For ease of presentation, we assume in the sequel that the flow geometry is cylindrical and that the flow field has the particular form $(0,0,u(x,y))$, which allows us to restrict the considerations to a two dimensional setting; the extension to three dimensions will be discussed briefly in section 5. Without loss of generality, we assume that measurements are available in the domain $D=(-1,1)^2$, which we call the *field of view*.

For a given radius function $R:[0,2\pi]\to\mathbb{R}_+$, we define the domain

$$\Omega_R=\{(r\cos\varphi,r\sin\varphi):0\leqslant r<R(\varphi),\ 0\leqslant\varphi\leqslant 2\pi\},\tag{1}$$

parametrized by R, and we denote by $\Omega^\dagger=\Omega_{R^\dagger}$ the true flow geometry. Throughout the presentation, we assume that

$$R^\dagger\in H^k_{\rm per}(0,2\pi)\ \text{with}\ \mathrm{r}_0\leqslant R(\varphi)\leqslant r_1\tag{2}$$

for some constants $2\leqslant k\leqslant 4$ and $0<r_0<r_1<1$, where $H^s_{\rm per}(0,2\pi)$ is the subspace of periodic functions in the Sobolev space $H^s(0,2\pi)$, $s\geqslant 0$. Let us note that the above assumptions imply in particular that $\Omega^\dagger$ is of class $C^{k-1,\alpha}$, compactly embedded in D, and star shaped with respect to the origin.

The geometry identification from possibly perturbed magnetic resonance images of the proton density can now be formulated as a nonlinear inverse problem

$$F(R)=m^\delta\qquad\text{on } D,\tag{3}$$

with forward operator $F:D(F)\subset H^2_{\rm per}(0,2\pi)\to L^2(D)$, $R\mapsto\chi_{\Omega_R}$ defined on the domain $D(F)=\{R\in H^2_{\rm per}(0,2\pi):r_0\leqslant R(\varphi)\leqslant r_1\}$. As usual, we assume that the perturbations in the data are bounded by

$$\|\chi_{\Omega^\dagger} - m^\delta\|_{L^2(D)} \leqslant \delta \tag{4}$$

and that knowledge of the noise level δ is available. For the stable approximation of solutions to problem (3), we consider Tikhonov regularization with the functional

$$J_\alpha^\delta(R) = \|F(R) - m^\delta\|_{L^2(D)}^2 + \alpha\|R\|_{H^2(0,2\pi)}^2. \tag{5}$$

We call $R_\alpha^\delta \in D(F)$ an *approximate minimizer* for regularization parameter $\alpha > 0$, if

$$J_\alpha^\delta(R_\alpha^\delta) \leqslant \inf_{R\in D(F)} J(R) + \delta^2. \tag{6}$$

Note that the operator F here is continuous but not differentiable and, therefore, standard convergence rate results about Tikhonov regularization, see [8, chapter 10], do not apply. Instead, we utilize recent results on Tikhonov regularization in Hilbert scales under conditional stability [6, 27], which allow us to prove the following assertions.

Theorem 2.1. *Assume that $R^\dagger \in H^k_{\rm per}(0,2\pi) \cap D(F)$, $2 \leqslant k \leqslant 4$. Then any approximate minimizer R_α^δ of the Tikhonov functional (5) with $\alpha = \delta^{4/k}$ satisfies*

$$\|F(R_\alpha^\delta) - \chi_{\Omega^\dagger}\|_{L^2(D)} \leqslant C\delta \quad \text{and} \quad \|R_\alpha^\delta - R^\dagger\|_{H^r(0,2\pi)} \leqslant C\delta^{1-r/k} \tag{7}$$

for $0 \leqslant r \leqslant 2$, with a constant C that only depends on the norm $\|R^\dagger\|_{H^k(0,2\pi)}$ of the true solution. The same estimates hold true, if α is chosen by a discrepancy principle, i.e.

$$\alpha = \max\{\alpha_0\, 2^{-n} : n \geqslant 0 \text{ such that } \|F(R_\alpha^\delta) - m^\delta\|_{L^2(D)} \leqslant 4\delta\}. \tag{8}$$

Proof. Note that $X_s = H^s_{\rm per}(0,2\pi)$, $s \in \mathbb{R}$ defines a Hilbert scale and $Y = L^2(D)$ is a Hilbert space. In view of the results in [6], it thus remains to establish a conditional stability estimate for the operator F. To do so, let us assume that $R, \widetilde R \in D(F)$ and define $r_{\min}(\varphi) = \min\{R(\varphi), \widetilde R(\varphi)\}$ and $r_{\max}(\varphi) = \max\{R(\varphi), \widetilde R(\varphi)\}$. Then

$$|F(R) - F(\widetilde R)|(r\cos\varphi, r\sin\varphi) = \begin{cases} 1, & \text{for } r_{\min}(\varphi) \leqslant r \leqslant r_{\max}(\varphi), \\ 0 & \text{else.} \end{cases}$$

This allows us to express the difference in the observations by

$$\begin{aligned}
\|F(R) - F(\widetilde R)\|_{L^2(D)}^2 &= \int_0^{2\pi}\int_0^{r_1} |F(R) - F(\widetilde R)|^2 r\,\mathrm{d}r\,\mathrm{d}\varphi = \int_0^{2\pi}\int_{r_{\min}(\varphi)}^{r_{\max}(\varphi)} r\,\mathrm{d}r\,\mathrm{d}\varphi \\
&= \frac{1}{2}\int_0^{2\pi} r_{\max}(\varphi)^2 - r_{\min}(\varphi)^2 \mathrm{d}\varphi = \frac{1}{2}\int_0^{2\pi} |R(\varphi) - \widetilde R(\varphi)|\,|R(\varphi) + \widetilde R(\varphi)|\,\mathrm{d}\varphi \\
&\geqslant \frac{1}{2}\int_0^{2\pi} |R(\varphi) - \widetilde R(\varphi)| 2r_0 \frac{|R(\varphi) - \widetilde R(\varphi)|}{|r_1 - r_0|}\,\mathrm{d}\varphi = \frac{r_0}{r_1 - r_0}\|R - \widetilde R\|_{L^2(0,2\pi)}^2.
\end{aligned}$$

Hence $\|R - \widetilde R\|_{L^2(0,2\pi)} \leqslant C\|F(R) - F(\widetilde R)\|_{L^2(D)}$ for all $R, \widetilde R \in D(F)$, i.e. the operator F satisfies a conditional Lipschitz stability estimate. The assertions of the theorem then follow from theorems 2.1 and 2.2 in [6] with $a = 0$, $s = 2$, $u = k$, and $\gamma = 1$. □

Remark 2.2. The theorem states that the geometry can be identified stably and accurately via Tikhonov regularization. Only a simple smoothness condition for the function $R^\dagger$, and thus on the domain $\Omega^\dagger$, is required to obtain a quantitative convergence result. If a bound $\|R^\dagger\|_{H^4(0,2\pi)} \leqslant C$ for the solution is available, then

$$\|R_\alpha^\delta - R^\dagger\|_{H^2(0,2\pi)} \leqslant \delta_R, \tag{9}$$

with $\delta_R = C\delta^{1/2}$ and we may assume that the bound δ_R is known for further computations. The results of [6] even provide more general estimates of the form

$$\|R_\alpha^\delta - R^\dagger\|_{H^r} \leqslant C\delta^{1-r/k}, \qquad 0 \leqslant r \leqslant s,$$

if regularization is performed in the norm of $H^s(0,2\pi)$ for $2 \leqslant s \leqslant k/2$ and with regularization parameter $\alpha = \delta^{2s/k}$. Hence, convergence rates arbitrarily close to one can, in principle, be obtained in any desired norm if the true solution $R^\dagger$ is sufficiently smooth and the regularization norm is chosen sufficiently strong.

3. Velocity approximation

Let us recall from equation (1) the definition of a domain Ω_R parametrized by a radius function $R \in D(F)$. Using the scaling transformation

$$\phi_R : (r\cos\varphi, r\sin\varphi) \mapsto (r_0\, r + (R(\varphi) - r_0)\, r^\eta) \cdot (\cos\varphi, \sin\varphi), \tag{10}$$

with $\eta \geqslant k \geqslant 2$ and k as in the previous section, we can express Ω_R equivalently as image $\Omega_R = \phi_R(B)$ of the unit disk $B = \{x \in \mathbb{R}^2 : |x| < 1\}$. Some analytical properties of this transformation are derived in appendix A. In the following, we assume that

$$R^\dagger, R_\alpha^\delta \in D(F), \quad R^\dagger \in H^4_{\text{per}}(0,2\pi), \quad \text{and} \quad \|R_\alpha^\delta - R^\dagger\|_{H^2(0,2\pi)} \leqslant \delta_R, \tag{11}$$

with known bound $\delta_R \leqslant C$; see the discussion in remark 2.2 For ease of notation, we write $\phi^\dagger = \phi_{R^\dagger}$, $\phi_\alpha^\delta = \phi_{R_\alpha^\delta}$, and denote by $\Omega^\dagger = \phi^\dagger(B)$ and $\Omega_\alpha^\delta = \phi_\alpha^\delta(B)$ the corresponding domains parametrized by the radius functions $R^\dagger$ and R_α^δ, respectively.

The velocity reconstruction from noisy velocity data u^ϵ can then be formulated compactly as a linear inverse problem over the reference domain, i.e.

$$Tv = u^\epsilon \circ \phi_\alpha^\delta \qquad \text{in } B, \tag{12}$$

with operator $T : H_0^1(B) \cap H^2(B) \to L^2(B)$ defined by $T(v) = v$, i.e. as simple embedding between Sobolev spaces. We assume that a bound on the data perturbations

$$\|u^\dagger - u^\epsilon\|_{L^2(D)} \leqslant \epsilon \tag{13}$$

is available, where $u^\dagger$ denotes the true velocity field to be reconstructed, and we require that $u^\dagger$ is piecewise smooth and vanishes outside $\Omega^\dagger$, i.e.

$$u^\dagger \in H^1(D), \qquad u^\dagger|_{\Omega^\dagger} \in H^3(\Omega^\dagger), \quad \text{and} \quad u^\dagger|_{D\setminus\Omega^\dagger} \equiv 0. \tag{14}$$

Let us note that these assumptions are reasonable, if the flow domain $\Omega^\dagger$ is smooth.

Remark 3.1. Observe that information about zero velocity at the boundary of the flow domain is encoded explicitly into the definition of the operator T. Due to the particular formulation (12) over the reference domain B, inexact knowledge about the flow domain is shifted

to the data $u^\epsilon \circ \phi_\alpha^\delta$ and the operator T is therefore independent of the geometry reconstruction. This simplifies the analysis given in the following. Let us note that invertibility of the transformation ϕ_α^δ is guaranteed by lemma A.4, which allows to associate to any approximate solution v of equation (12) on the reference domain a velocity field $u = v \circ (\phi_\alpha^\delta)^{-1}$ in physical space.

For the stable solution of the nonlinear inverse problem (12), we again consider Tikhonov regularization and we define the regularized approximations by

$$v_{\alpha,\beta}^{\delta,\epsilon} = \arg\min_{v \in D(T)} \|Tv - u^\epsilon \circ \phi_\alpha^\delta\|_{L^2(B)}^2 + \beta \|\Delta v\|_{L^2(B)}^2, \tag{15}$$

where $D(T) = H^2(B) \cap H_0^1(B)$ by definition. For our further analysis, we will require two auxiliary results that we will present next. As a first step, we derive an estimate for the data error in the reference domain.

Lemma 3.2. *Let the assumptions (11), (13) and (14) hold. Then*

$$\|u^\dagger \circ \phi^\dagger - u^\epsilon \circ \phi_\alpha^\delta\|_{L^2(B)} \leqslant \delta_U \tag{16}$$

with $\delta_U = C(\delta_R^{1/2} \|u^\dagger\|_{H^3(\Omega^\dagger)} + \epsilon)$ *and a constant* C *that can be computed explicitly.*

Proof. By the integral transformation theorem we have

$$\begin{aligned}\|u^\dagger \circ \phi^\dagger - u^\epsilon \circ \phi_\alpha^\delta\|_{L^2(B)} &\leqslant \|\det(J_\alpha^\delta)^{-1}\|_{L^\infty(B)} \|u^\dagger \circ \phi^\dagger \circ (\phi_\alpha^\delta)^{-1} - u^\epsilon\|_{L^2(\Omega_\alpha^\delta)} \\ &\leqslant C(\|u^\dagger \circ \phi^\dagger \circ (\phi_\alpha^\delta)^{-1} - u^\dagger\|_{L^2(\Omega_\alpha^\delta)} + \|u^\dagger - u^\epsilon\|_{L^2(\Omega_\alpha^\delta)}),\end{aligned}$$

where we used lemma A.4 to estimate the Jacobian J_α^δ of the transformation ϕ_α^δ in the second step. The last term can then be readily estimated by the bound (13) on the data noise. The first term on the right hand side can further be split as

$$\begin{aligned}&\|u^\dagger \circ \phi^\dagger \circ (\phi_\alpha^\delta)^{-1} - u^\dagger\|_{L^2(\Omega_\alpha^\delta)} \\ &\leqslant \|u^\dagger \circ \phi^\dagger \circ (\phi_\alpha^\delta)^{-1} - u^\dagger\|_{L^2(\Omega_\alpha^\delta \cap \Omega^\dagger)} + \|u^\dagger \circ \phi^\dagger \circ (\phi_\alpha^\delta)^{-1}\|_{L^2(\Omega_\alpha^\delta \setminus \Omega^\dagger)} = (i) + (ii),\end{aligned}$$

where we used $u^\dagger \equiv 0$ in $\Omega_\alpha^\delta \setminus \Omega^\dagger$ which follows from assumption (14). From the smoothness of R_α^δ, $R^\dagger$, and $u^\dagger$, and using the bound on the difference of the inverse transformations $(\phi_\alpha^\delta)^{-1}$ and $(\phi^\dagger)^{-1}$ provided by lemma A.5, we then obtain

$$\begin{aligned}(i) &= \|u^\dagger \circ \phi^\dagger \circ (\phi_\alpha^\delta)^{-1} - u^\dagger \circ \phi^\dagger \circ (\phi^\dagger)^{-1}\|_{L^2(\Omega_\alpha^\delta \cap \Omega^\dagger)} \\ &\leqslant \|u^\dagger \circ \phi^\dagger\|_{W^{1,\infty}(B)} \|(\phi_\alpha^\delta)^{-1} - (\phi^\dagger)^{-1}\|_{L^\infty(\Omega_\alpha^\delta \cap \Omega^\dagger)} |\Omega_\alpha^\delta \cap \Omega^\dagger|^{1/2} \\ &\leqslant C\|\phi^\dagger\|_{W^{1,\infty}(B)} \|u^\dagger\|_{H^3(\Omega^\dagger)} \delta_R \leqslant C\|u^\dagger\|_{H^3(\Omega^\dagger)} \delta_R.\end{aligned}$$

Observe that $\|\phi^\dagger\|_{W^{1,\infty}(B)} \leqslant C\|R^\dagger\|_{W^{1,\infty}(0,2\pi)} \leqslant C'\|R^\dagger\|_{H^2(0,2\pi)}$ by definition (10) of the transformation and continuous embedding. Using lemma A.1 and assumption (11), we can control the area $|\Omega_\alpha^\delta \setminus \Omega^\dagger|$ of the geometry mismatch by δ_R, which allows us to bound the remaining term in the above estimate by

$$\|u^\dagger \circ \phi^\dagger \circ (\phi_\alpha^\delta)^{-1}\|_{L^2(\Omega_\alpha^\delta \setminus \Omega^\dagger)} \leqslant \|u^\dagger\|_{L^\infty(D)} |\Omega_\alpha^\delta \setminus \Omega^\dagger|^{1/2} \leqslant C \|u^\dagger\|_{H^3(\Omega^\dagger)} \delta_R^{1/2}.$$

Note that the constants C in the above estimates are generic and independent of ϵ and δ. A combination of the bounds then yields the assertion of the lemma. □

Remark 3.3. Following remark 2.2 and the arguments used in the proof above, the bound δ_U in (16) is computable in terms of the data noise levels δ and ϵ in (4) and (13), if bounds on $\|R^\dagger\|_{H^4(0,2\pi)}$ and $\|u^\dagger\|_{H^3(\Omega^\dagger)}$ are available. For our further computations, we may thus assume that δ_U is known.

As a next step, we interpret standard smoothness assumptions on $u^\dagger$ in terms of the operator T, which will allow us to utilize simple source conditions below.

Lemma 3.4. *Let assumptions (11) and (14) hold and define* $v^\dagger := u^\dagger \circ \phi^\dagger$.

Then $v^\dagger \in R((T^*T)^\mu)$ *for all* $\mu < 1/8$. *However,* $v^\dagger \notin R((T^*T)^{1/8})$, *in general.*

Proof. We equip $D(T) = H^2(B) \cap H_0^1(B)$ with the norm $\|v\| := \|\Delta v\|_{L^2(B)}$. Then for arbitrary $v \in H^2(B) \cap H_0^1(B)$ and $f \in L^2(B)$, we have

$$(T^*f, v)_{H^2(B)\cap H_0^1(B)} = (\Delta T^*f, \Delta v)_{L^2(B)} = (f, Tv)_{L^2(B)} = (f, v)_{L^2(B)}.$$

Thus $w = T^*f$ is given as the unique solution of the boundary value problem

$$\Delta^2 v = f \quad \text{in } B \qquad \text{with} \qquad v = 0 \quad \text{and} \quad \Delta v = 0 \qquad \text{on } \partial B.$$

From standard elliptic regularity theory [9], we can conclude that $w = T^*f \in H^4(B)$ for any $f \in L^2(B)$. Using $\mathcal{R}((T^*T)^{1/2}) = \mathcal{R}(T^*)$, see [8, theorem 2.6], we thus arrive at

$$\mathcal{R}((T^*T)^0) = \{v \in H^2(B) \mid v = 0 \text{ on } \partial B\},$$
$$\mathcal{R}((T^*T)^{1/2}) = \{v \in H^4(B) \mid v = \Delta v = 0 \text{ on } \partial B\}.$$

From the regularity assumptions on $u^\dagger$ and $R^\dagger$, we deduce that $v^\dagger \in H^3(B)$ with $v^\dagger = 0$ on ∂B, but $\Delta v^\dagger \neq 0$ on ∂B, in general. By interpolation of Sobolev spaces [13], we thus deduce that $v^\dagger \in R((T^*T)^\mu)$ for $\mu < 1/8$, but not for $\mu \geqslant 1/8$, in general. □

Remark 3.5. A range condition $v^\dagger \in \mathcal{R}((T^*T)^\mu)$ would hold with $\mu = 1/4$, if $\Delta v^\dagger = 0$ at ∂B would be valid additionally; this can however not be expected in general. The limiting factor for the regularity index μ in the range condition, therefore, is the mismatch of the higher order boundary conditions. This could be circumvented by choosing a different equivalent norm on $H^2(B) \cap H_0^1(B)$; see [18] for details.

From standard results about Tikhonov regularization in Hilbert spaces for linear inverse problems [8], we can now immediately conclude the following results.

Theorem 3.6. *Let assumptions (11)–(14) hold and let* $v_{\alpha,\beta}^{\delta,\epsilon}$ *be defined by (15) with regularization parameter* $\beta = \delta_U^{2/(2\mu+1)}$. *Then*

$$\|v_{\alpha,\beta}^{\delta,\epsilon} - v^\dagger\|_{H^2(B)} \leqslant C\delta_U^{\frac{2\mu}{2\mu+1}} \quad \text{for all} \quad 0 \leqslant \mu < 1/8. \tag{17}$$

The same estimates hold for a-posteriori parameter choice by the discrepancy principle

$$\beta = \max\{\beta_0\, 2^{-n} : n \geqslant 0 \text{ and such that } \|v_{\alpha,\beta}^{\delta,\epsilon} - v^\dagger\| \leqslant 2\delta_U\}. \tag{18}$$

Corresponding bounds for the error in the velocity u can be obtained, in principle, by back transformation into physical domain and some elementary computations. Let us close this section with a remark indicating some natural generalizations.

Remark 3.7. If $u^\dagger$ is sufficiently smooth and the functional in (15) is replaced by

$$\|Tv - u^\epsilon \circ \phi_\alpha^\delta\|_{L^2(B)}^2 + \beta\|\Delta^t v\|_{L^2(B)}^2,$$

with $T : D(T) \subset H^{2t}(B) \cap H_0^1(B) \to L^2(B)$ defined by $Tv = v$ and $t \geqslant 1$ sufficiently large, one could, in principle, obtain any rate $2\mu/(2\mu + 1)$ sufficiently close to one. Further note that the data residual could also be measured in physical space. The regularized approximate solution is then defined by

$$\widetilde{v}_{\alpha,\beta}^{\delta,\epsilon} = \arg \min_{v \in D(\widetilde{T})} \|\widetilde{T}v - u^\epsilon\|_{L^2(\Omega_\alpha^\delta)}^2 + \beta\|\Delta^t v\|_{L^2(B)}^2,$$

with operator $\widetilde{T} : H^2(B) \cap H_0^1(B) \to L^2(\Omega_\alpha^\delta)$ given by $\widetilde{T}v = v \circ (\phi_\alpha^\delta)^{-1}$. This simply amounts to a change to an equivalent norm in the data space. A quick inspection of the arguments in the above proof reveals that the assertions of theorem 3.6 remain valid also for this choice of regularization method, which is more easy to implement and will thus be used in our numerical tests in section 6.

4. Computation of the wall shear stress

Let $R \in \mathcal{D}(F)$ be a given radius function with associated transformation ϕ_R and let v be a given velocity field defined on the reference domain B. For ease of notation, we assume that fluid viscosity is normalized, and define the associated wall shear stress by

$$\tau_R(v)(\varphi) = -n_R(\varphi) \cdot J_R(\cos\varphi, \sin\varphi)^{-1} \cdot (\nabla v)(\cos\varphi, \sin\varphi), \tag{19}$$

where J_R is the Jacobian of ϕ_R, and $n_R(\varphi)$ is the outward pointing unit normal vector at the corresponding point $(R(\varphi)\cos\varphi, R(\varphi)\sin\varphi) \in \partial\Omega_R$ in the physical domain. Let us note that $n_R(\varphi)$ can be expressed explicitly by

$$n_R(\varphi) = \frac{(R(\varphi)\cos\varphi + R'(\varphi)\sin\varphi, R(\varphi)\sin\varphi - R'(\varphi)\cos\varphi)}{\sqrt{(R(\varphi))^2 + (R'(\varphi))^2}}. \tag{20}$$

For ease of notation, we will identify ∂B with the interval $(0, 2\pi)$ in the sequel. In addition, we again define symbols $\tau_{\alpha,\beta}^{\delta,\epsilon} = \tau_{R_\alpha^\delta}(v_{\alpha,\beta}^{\delta,\epsilon})$ and $\tau^\dagger = \tau_{R^\dagger}(v^\dagger)$ where $v^\dagger = u^\dagger \circ \phi^\dagger$. A combination of the results derived so far and some elementary geometric computations now leads to the following assertion.

Theorem 4.1. *Let the assumptions of theorem 3.7 hold. Then*

$$\|\tau_{\alpha,\beta}^{\delta,\epsilon} - \tau^\dagger\|_{L^2(0,2\pi)} \leqslant C(\delta_R + \delta_U^{(2\mu)/(2\mu+1)}) \quad \text{for all} \quad 0 \leqslant \mu < 1/8. \tag{21}$$

Proof. We use the definition of $\tau_R(v)$ and decompose the error into the three parts

$$\begin{aligned}\|\tau^{\delta,\epsilon}_{\alpha,\beta} - \tau^\dagger\|_{L^2(0,2\pi)} &= \|n_{R^\delta_\alpha} J^{-1}_{R^\delta_\alpha} \nabla v^{\delta,\epsilon}_{\alpha,\beta} - n_{R^\dagger} J^{-1}_{R^\dagger} \nabla v^\dagger\|_{L^2(\partial B)} \\ &\leqslant \|(n_{R^\delta_\alpha} - n_{R^\dagger}) J^{-1}_{R^\delta_\alpha} \nabla v^{\delta,\epsilon}_{\alpha,\beta}\|_{L^2(\partial B))} + \|n_{R^\dagger}(J^{-1}_{R^\delta_\alpha} - J^{-1}_{R^\dagger}) \nabla v^{\delta,\epsilon}_{\alpha,\beta}\|_{L^2(\partial B))} \\ &\quad + \|n_{R^\dagger} J^{-1}_{R^\dagger}(\nabla v^{\delta,\epsilon}_{\alpha,\beta} - \nabla v^\dagger)\|_{L^2(\partial B))} = (i) + (ii) + (iii).\end{aligned}$$

Using lemmas A.2 and A.3, and the embedding of Sobolev spaces, we obtain

$$\begin{aligned}(i) &\leqslant \|n_{R^\delta_\alpha} - n_{R^\dagger}\|_{L^\infty(\partial B))} \|J^{-1}_{R^\delta_\alpha}\|_{L^\infty(\partial B))} \|\nabla v^{\delta,\epsilon}_{\alpha,\beta}\|_{L^2(\partial B))} \\ &\leqslant C\|R^\delta_\alpha - R^\dagger\|_{H^2(0,2\pi)} \|R^\delta_\alpha\|_{H^2(0,2\pi)} \|v^{\delta,\epsilon}_{\alpha,\beta}\|_{H^2(B)} \leqslant C\delta_R.\end{aligned}$$

By the geometric arguments of lemma A.5, the second term can be estimated by

$$\begin{aligned}(ii) &\leqslant \|n_{R^\dagger}\|_{L^\infty(\partial B))} \|J^{-1}_{R^\delta_\alpha} - J^{-1}_{R^\dagger}\|_{L^\infty(\partial B))} \|\nabla v^{\delta,\epsilon}_{\alpha,\beta}\|_{L^2(\partial B))} \\ &\leqslant C\|R^\delta_\alpha - R^\dagger\|_{H^2(0,2\pi)} \|v^{\delta,\epsilon}_{\alpha,\beta}\|_{H^2(B)} \leqslant C\delta_R.\end{aligned}$$

With the help of the results of the previous section, the third term, which measures the amplification of the velocity approximation error, can be bounded by

$$\begin{aligned}(iii) &\leqslant \|n_{R^\dagger}\|_{L^\infty(\partial B))} \|J^{-1}_{R^\dagger}\|_{L^\infty(\partial B))} \|\nabla v^{\delta,\epsilon}_{\alpha,\beta} - \nabla v^\dagger\|_{L^2(\partial B))} \\ &\leqslant C\|R^\dagger\|_{H^2(0,2\pi)} \|v^{\delta,\epsilon}_{\alpha,\beta} - v^\dagger\|_{H^2(B)} \leqslant C\delta_U^{(2\mu)/(2\mu+1)}.\end{aligned}$$

The assertion of the theorem then follows by combination of these estimates. □

Remark 4.2. Let us note that, following the considerations of remarks 2.2 and 3.7, one could in principle again obtain convergence rates arbitrarily close to one, if the true flow geometry and velocity are sufficiently smooth and the regularization terms in the Tikhonov functionals (5) and (15) are chosen sufficiently strong. The main observation of the previous theorem therefore is, that it is possible to obtain a quantitative estimate under reasonable smoothness assumptions.

5. Remarks on the extension to three dimensions

For a three-dimensional flow, the wall shear stress is a tensor defined by

$$\tau = -\mu\left(\nabla u + (\nabla u)^T\right) \cdot n,$$

where μ is the dynamic viscosity, u is the velocity vector, and n the outer unit normal vector at the vessel wall. If appropriate measurements of the proton density and of all three velocity components are available, then the reconstruction approach and the theoretical results presented in the previous sections can be generalized almost verbatim to the three dimensional setting; only the computational realization becomes more complicated. Note that the geometry and velocity reconstruction naturally decompose into a sequence of two-dimensional inverse problems for the individual cross-sections for fixed coordinate z in the flow direction. To ensure continuity of the reconstructions with respect to the z-coordinate, one has to employ

regularization also in the z-direction, which fully couples the problems for the individual cross-sections. The additional computational complexity due to this coupling can be overcome by a Kaczmarz strategy [11, 14], which allows to reduce the numerical solution to the iterated solution of two-dimensional problems for the individual cross-sections. A detailed investigation of these computational aspects is, however, not in the scope of the current paper and will be given elsewhere.

6. Numerical validation

In order to demonstrate the viability of our approach, we now report about the reconstruction of flow geometry, flow velocity, and wall shear stress from experimental data obtained in a clinical whole-body 3 T magnetic resonance imaging scanner (Prisma, Siemens Healthcare, Erlangen) at the University Medical Center Freiburg. As a test case, we consider the flow of water through a cylindrical pipe with constant diameter $d = 25.885\,\text{mm}$ at a constant flow rate of about $6\,\text{l}\,\text{min}^{-1}$ and a temperature of about 22 °C; details about the experimental setup are described in [1]. The Reynolds number here is about 5300 and the experiment thus amounts to a turbulent flow with steep velocity gradients in the boundary layer. For our reconstruction procedures, we utilize magnetic resonance images of proton density and the axial flow velocity acquired with different resolutions corresponding to in plane voxel sizes of $h = 1.5\,\text{mm}$ to $h = 0.3\,\text{mm}$. Due to the axisymmetic geometry, we expect an almost radially symmetric flow, but this *a priori* knowledge will not be utilized in our computational tests.

Remark 6.1. Up to a simple translation, the exact geometry $\Omega^\dagger = \phi^\dagger(B)$ of the pipe is known here. A reference solution u^{ref} for the flow velocity can thus be computed by numerical simulation [12] and will be used for comparison with our results. Let us emphasize that this reference solution represents a time averaged velocity field, in which all temporal fluctuations are suppressed. The experimental data, on the other hand, contain such turbulent fluctuations; see figure 3. In addition, also the flow conditions, e.g. temperature and flow rate, do not match exactly with the simulation data. One therefore cannot expect to get a perfect fit to the simulated reference velocity data.

Remark 6.2. The following test problems are concerned with two-dimensional data at a realisitc and hence relatively coarse resolution. The reconstructions of geometry and velocity can therefore computed in about one second in all our numerical tests, whereas the measurement times are in the order of minutes. We therefore only sketch the basic ingredients of our implementation and do not discuss in detail computational efficiency of our algorithms. This aspect will ceratainly play an important role when considering three or four dimensional data sets. In the following test, we do, however, compare the quality of reconstructions obtained with our algorithms with those obtained by more traditional methods.

6.1. Geometry identification

For the geometry identification, we utilize the standard magnetic resonance images of the proton density. After a simple scaling procedure, see appendix B for details, the data can be interpreted as

Table 1. Relative reconstruction errors $\|R_\alpha^\delta - R^\dagger\|_{H^2(0,2\pi)}/\|R^\dagger\|_{H^2(0,2\pi)}$ for different data resolutions h and regularization parameters α; optimal results in bold.

$h \setminus \alpha$	0.16	0.08	0.04	0.02	0.01
1.00	0.0220	0.0117	**0.0098**	0.0128	0.0194
0.75	0.0161	**0.0111**	0.0118	0.0155	0.0215
0.60	0.0132	**0.0086**	0.0089	0.0129	0.0201
0.43	0.0104	**0.0079**	0.0090	0.0121	0.0172
0.30	0.0064	**0.0053**	0.0063	0.0087	0.0127

$$m^\delta|_{V_i} = \frac{1}{|V_i|}\int_{V_i} \chi_{\Omega^\dagger}(x)\mathrm{d}x + \text{noise},$$

where V_i denotes the ith voxel of size $h \times h$ in the measurement array. The action of the forward operator for our computational tests is then defined as

$$F_{\gamma,h}(R)|_{V_i} = \frac{1}{|V_i|}\sum_{\xi_\ell \in V_i} H_\gamma(R(\varphi(\xi_\ell)) - |\xi_\ell|)\, w_\ell, \tag{22}$$

where $H_\gamma(x) = \frac{1}{\pi}\arctan\left(\frac{x}{\gamma}\right) + \frac{1}{2}$ is a smooth approximation of the Heaviside function with $\gamma > 0$ denoting a regularization parameter, and (ξ_ℓ, w_ℓ) are quadrature points and weights for approximating the integral $\int_D f(x)\mathrm{d}x \approx \sum_\ell f(\xi_\ell)w_\ell$. In our computational tests, we then minimize the Tikhonov functional

$$J^\delta_{\alpha,\gamma,h}(R) = \|F_{\gamma,h}(R) - m^\delta\|^2_{h,D} + \alpha\,\|R\|^2_{H^2(0,2\pi)} \tag{23}$$

over the finite dimensional space of radius functions

$$V_N = \{R_N \in H^2_{\mathrm{per}}(0,2\pi)\,|\,R_N(\varphi) = b_0 + \sum_{k=1}^N a_k \sin(k\varphi) + b_k\cos(k\varphi)\} \cap D(F).$$

Here $\|m\|^2_{h,D} = \frac{|D|}{M}\sum_{i=1}^M m_i^2$ is used to approximate the corresponding data misfit term in the Tikhonov functional (5). Let us note that for $\gamma > 0$, the discretized forward operator $F_{\gamma,h}$ and also the discretized Tikhonov functional $J^\delta_{\alpha,\gamma,h}$ are continuously differentiable. Moreover, the derivative of $F_{\gamma,h}$ and consequently the gradient of $J^\delta_{\alpha,\gamma,h}$ can be computed exactly on the discrete level. Therefore, a projected Gauss–Newton method [7, 11] can be used for the minimization process.

For our computational tests, the center of the coordinate system was chosen as the barycenter of the measurement data m^δ and the true radius was $R^\dagger = 12.94$ mm. In table 1, we display the relative errors $\|R_\alpha^\delta - R^\dagger\|_{H^2(0,2\pi)}/\|R^\dagger\|_{H^2(0,2\pi)}$ obtained for measurements acquired with different data resolution h, and for different choices of the regularization parameter α.

By visual inspection of the proton density images, compare with figure 2, one can verify that the information content about geometry increases with increasing data resolution, and we observe a corresponding decrease in geometry reconstruction errors. Further note that the reconstructions are very stable with respect to the choice of the regularization parameter and

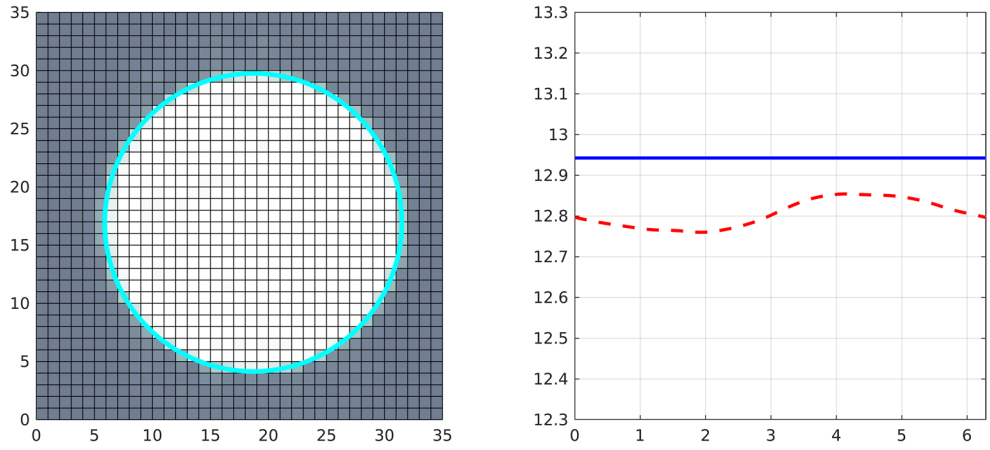

Figure 1. Proton density data ($h = 1$ mm) with reconstructed geometry (left); radius functions R_α^δ (dashed red) and $R^\dagger$ (solid blue); axis labeling in mm.

the optimal regularization parameters, i.e. those for which the error is minimal, are practically independent of the data resolution.

In figure 1, we display one of the data sets used for our computations, together with the reconstructed geometry and the radius functions $R^\dagger$ and R_α^δ obtained in our numerical tests. The maximal error in the reconstructed radius is about 0.15 mm, which is substantially less than the voxel size $h = 1$mm of the data. This illustrates that sub-pixel resolution can be obtained by the proposed geometry reconstruction procedure.

For comparison with standard image segmentation tools, we apply a Laplacian filter to the proton density measurements, i.e. we compute

$$(\Delta_h m^\delta)_{i,j} = m^\delta_{i-1,j} + m^\delta_{i+1,j} + m^\delta_{i,j-1} + m^\delta_{i,j+1} - 4m^\delta_{i,j}.$$

The absolute values $|\Delta_h m^\delta|$ of the filtered data serves as an indicator for the location of the geometry interface [2]. In figure 2 we display the corresponding results for two data resolutions and compare them with our parametric estimation of the geometry. The edge detector $|\Delta_h m^\delta|$ yields high values in a region around the boundary of the flow domain with a width of about 3 voxels. As a consequence, the prediction of the interface obtained by the edge detection filter becomes sharper when increasing the data resolution. Let us note that the parametric estimation obtained by our algorithm yields a very good fit to the center of the interface area predicted by the edge detection algorithm for both data resolutions. A similar parametric approximation or the flow boundary could also be obtained from $|\Delta_h m^\delta|$ by some sort of least squares fitting.

6.2. Velocity approximation

We now turn to the reconstruction of the velocity field, for which we utilize phase-contrast magnetic resonance imaging data [15, 22]; also see appendix B. Let $\Omega_\alpha^\delta = \phi_\alpha^\delta(B)$ denote the approximation of the flow domain obtained with the radius function R_α^δ reconstructed in the first step with α chosen as the best regularization parameter according to table 1. For voxels V_i lying at least partially in the flow domain, i.e. with $|V_i \cap \Omega_\alpha^\delta| > 0$, the measurements can be interpreted as

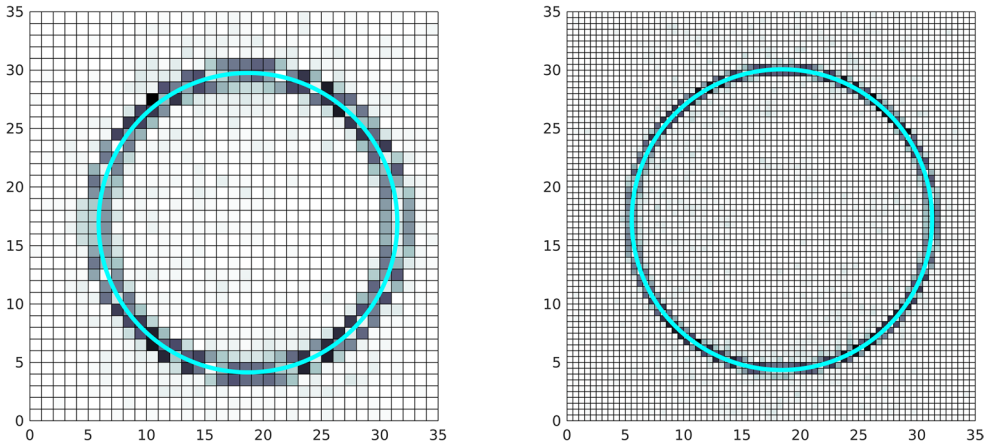

Figure 2. Absolute values $|\Delta_h m^\delta|$ of the Laplace filtered proton density measurements with resolutions $h = 1\,\text{mm}$ (left) and $h = 0.5\,\text{mm}$ (right). For comparison, we also desply the parametric reconstructions of the geometry by our algorithm (cyan).

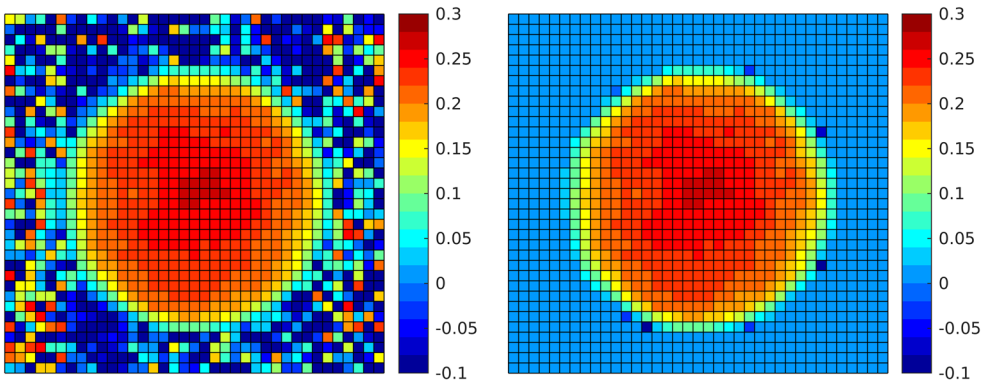

Figure 3. Velocity raw data u^ϵ with large noise outside the flow domain (left) and truncated velocity raw data actually used in the reconstruction (right).

$$u^\epsilon|_{V_i} = \frac{1}{|V_i \cap \Omega_\alpha^\delta|} \int_{V_i \cap \Omega_\alpha^\delta} u^\dagger(x)\mathrm{d}x + \text{noise}.$$

The remaining voxels only contain information about the noise and will not be used in the reconstruction; see figure 3 and the remarks given in appendix B.

Following remark 3.7, we define the corresponding forward operator mapping to the physical domain by $\widetilde{T}_h : H^2(B) \cap H_0^1(B) \to L^2(\Omega_\alpha^\delta)$ with

$$\widetilde{T}_h(v)|_{V_i} = \frac{1}{|V_i \cap \Omega_\alpha^\delta|} \int_{V_i \cap \Omega_\alpha^\delta} v \circ (\phi_\alpha^\delta)^{-1}(x)\mathrm{d}x.$$

Table 2. Relative reconstruction errors $\|\widehat{v}^{\delta,\epsilon}_{\alpha,\beta} - v^{\text{ref}}\|_{H^2(B)}/\|v^{\text{ref}}\|_{H^2(B)}$, with $v^{\text{ref}} = u^{\text{ref}} \circ \phi^\dagger$ denoting the simulated velocity on the reference domain, for different data resolutions h and regularization parameters β; optimal results in bold.

$h \setminus \beta$	$3.2 \cdot 10^{-4}$	$1.6 \cdot 10^{-4}$	$8.0 \cdot 10^{-5}$	$4.0 \cdot 10^{-5}$	$2.0 \cdot 10^{-5}$
1.00	0.3815	0.2661	**0.1818**	0.2249	0.3985
0.75	0.3317	0.2233	**0.1926**	0.2912	0.4541
0.60	0.3377	0.2313	**0.1813**	0.2507	0.3899
0.43	0.3098	0.2011	**0.1795**	0.2851	0.4478
0.30	0.3245	0.2090	**0.1518**	0.2106	0.3190

Note that only voxels V_i with $|V_i \cap \Omega^\delta_\alpha| > 0$ are required in the definition of $\widetilde{T}_h$. For the actual computations, we approximate the integral in the definition of $\widetilde{T}_h$ by numerical quadrature, and obtain

$$\widehat{T}_h(v)|_{V_i} = \frac{1}{|V_i \cap \Omega^\delta_\alpha|} \sum_{\xi_\ell \in V_i \cap \Omega^\delta_\alpha} v \circ (\phi^\delta_\alpha)^{-1}(\xi_\ell) w_\ell,$$

where (ξ_ℓ, w_ℓ) again denote appropriate quadrature points and weights. The regularized approximation for the velocity field in the reference domain is then defined as the minimizer of the Tikhonov functional

$$\widehat{v}^{\delta,\epsilon}_{\alpha,\beta} = \arg\min_{v \in V_L} \|\widehat{T}_h v - u^\epsilon\|^2_{h,\Omega^\delta_\alpha} + \beta \|\Delta v\|^2_{L^2(B)}, \tag{24}$$

over the space $V_L = \text{span}\{v \in H^1_0(B) | -\Delta v = \lambda v \text{ for some } \lambda \leqslant L\}$ of eigen functions of the Dirichlet Laplace operator on the unit disk. Here $\|u\|^2_{h,\Omega^\delta_\alpha} := \sum_{i=1}^M |u_i|^2 |V_i \cap \Omega^\delta_\alpha|$ is used as the natural approximation for the norm in the data misfit term in (24). The solution $\widehat{v}^{\delta,\epsilon}_{\alpha,\beta}$ of the regularized least-squares problem can now be computed efficiently by Cholesky factorization or the conjugate gradient method. In table 2, we display the reconstruction errors obtained with our algorithm for different data resolutions h and regularization parameters β.

Recall that u^{ref}, which was obtained by numerical simulation, corresponds to a time averaged velocity field and therefore does not contain temporal fluctuations that are present in the measurements; see figure 4. This explains the relatively large errors in table 2 and their independence of the data resolution. The optimal regularization parameters β are again independent of the voxel size h used in the data acquisition. There is a slight improvement of the estimate with increasing data resolution. Note, that the signal amplitude is related to the amount of fluid in some voxel; see appendix B.

Remark 6.3. Let us note that signal-to-noise ratios usually decrease with increasing data resolution. By local averaging, one can however always obtain data with better signal-to-noise rations but coarse resolution. The overall information content of the data will therefore always increase with increasing data resolution. Furthermore, the signal-to-noise ratio is particularly low in boundary voxels which are only partially filled by the fluid; this is known as partial volume effect [26]. In our approach, these voxels, however, have a low weight due to the definition of the data fitting term in (24).

A quick comparison with the raw data, depicted In figure 4, we display the reference velocity $v^{\text{ref}} = u^{\text{ref}} \circ \phi^\dagger$ obtained by simulation and transformation with the the numerical reconstructions $\widehat{v}^{\delta,\epsilon}_{\alpha,\beta}$ obtained with our approach. A quick comparison with the raw data depicted

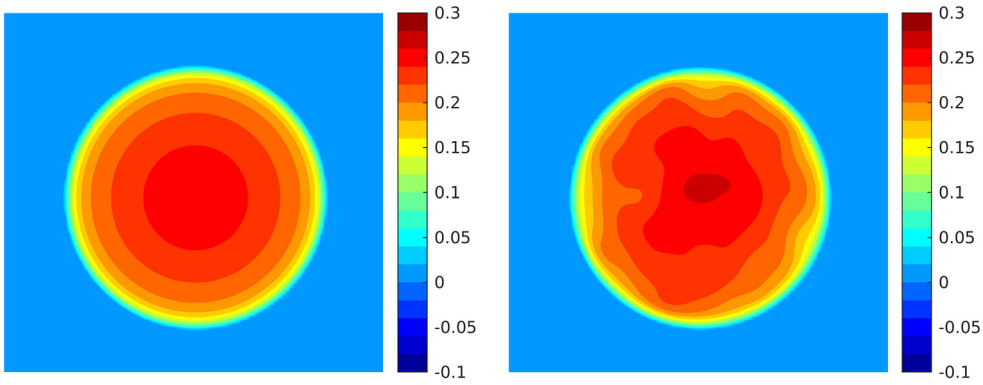

Figure 4. Reference velocity $v^{\text{ref}} = u^{\text{ref}} \circ \phi^{\dagger}$ (left) obtained by simulation and reconstructed velocity $\widehat{v}^{\delta,\epsilon}_{\alpha,\beta}$ (right) for data resolution $h = 1\,\text{mm}$ and $\beta = 8.0 \cdot 10^{-5}$.

in figure 3 shows that the deviations from radial symmetry in the data, most probably caused by instationarity of the turbulent flow, are correctly represented in our reconstructions, while the simulated data are perfectly symmetric due to artificial time averaging. Apart from these differences, the reconstruction is in good agreement with the reference solution.

Let us again compare our results to those obtained by more standard approaches, e.g. Tikhonov regularization. Here the velocity approximation is defined by the unique minimizer $u^{\epsilon}_{\text{std},\beta}$ of the Tikhonov functional

$$J_{\text{std}}(u) = \|u - u^{\epsilon}\|^2_{L^2(D)} + \beta \, \|u\|^2_{H^2(D)} \tag{25}$$

in the Hilbert space $H^2(D) \cap H^1_0(D)$, where D is the field of view, u^{ϵ} the voxel-wise constant measured velocity data, and β the regularization parameter. The problem is approximated on a fine grid with 10×10 points per voxel and appropriate finite differences and quadrature rules are used to approximate the required derivatives and integrals. The simulated velocity field u^{ref} is interpolated to the same grid and the errors of these reconstructions are listed in table 3. To allow for a fair comparison with our approach, we consider only errors in the flow domain Ω^{δ}_{α}. Let us note that due to a different scaling of the flow domain, the optimal regularization parameters β are rather small here. A quick comparison with the result of table 2 reveals that the errors that can be obtained by standard Tikhonov regularization are substantially larger than those of our approach. This can be explained as follows: due to the kink of the true velocity field u at the flow boundary, the exact velocity is not smooth on D and therefore cannot be approximated well by smooth functions. In our approach, this non-smoothness is avoided by explicitly restricting the reconstructions to the flow geometry.

6.3. Computation of the wall shear stress

As a final step in our tests, we now utilize the reconstructed radius function R^{δ}_{α} and velocity fields $v^{\delta,\epsilon}_{\alpha,\beta}$ to compute the approximation $\tau^{\delta,\epsilon}_{\alpha,\beta}$ for the wall shear stress via (19). In table 4, we display the results obtained for optimal α and $\beta = 1.6 \cdot 10^{-4}$. Let us note that most part of the error stems from perturbations in higher modes, which can be suppressed efficiently by application of a low-pass filter. In figure 5, we plot the reconstruction of the wall shear stress $\tau^{\delta,\epsilon}_{\alpha,\beta}$ and its constant approximation $\overline{\tau}^{\delta,\epsilon}_{\alpha,\beta}$ against the reference value τ^{ref} obtained from numerical

Table 3. Relative reconstruction errors $\|u^{\epsilon}_{\mathrm{std},\beta} - u^{\mathrm{ref}}\|_{H^2(\Omega^{\delta}_{\alpha})} / \|u^{\mathrm{ref}}\|_{H^2(\Omega^{\delta}_{\alpha})}$ for Tikhonov regularization obtained for different data resolutions h and regularization parameters β; optimal results in bold.

$h \setminus \beta$	$3.2 \cdot 10^{-14}$	$1.6 \cdot 10^{-14}$	$8.0 \cdot 10^{-15}$	$4.0 \cdot 10^{-15}$	$2.0 \cdot 10^{-15}$
1.00	0.5821	**0.5716**	0.5719	0.5899	0.6384
0.75	0.5261	0.5021	**0.4898**	0.4957	0.5294
0.60	0.5150	0.4852	0.4635	**0.4552**	0.4681
0.43	0.5067	0.4731	0.4468	**0.4335**	0.4430
0.30	0.5126	0.4805	0.4546	**0.4389**	0.4408

Table 4. Relative errors $\|\tau^{\delta,\epsilon}_{\alpha,\beta} - \tau^{\dagger}\|_{L^2(0,2\pi)}$ in the reconstruction of the wall shear stress by our approach for different data resolutions.

h	1.00	0.75	0.60	0.43	0.30
$\|\tau^{\delta,\epsilon}_{\alpha,\beta} - \tau^{\dagger}\|_{L^2(0,2\pi)}$	0.0789	0.0385	0.0391	0.0264	0.0405

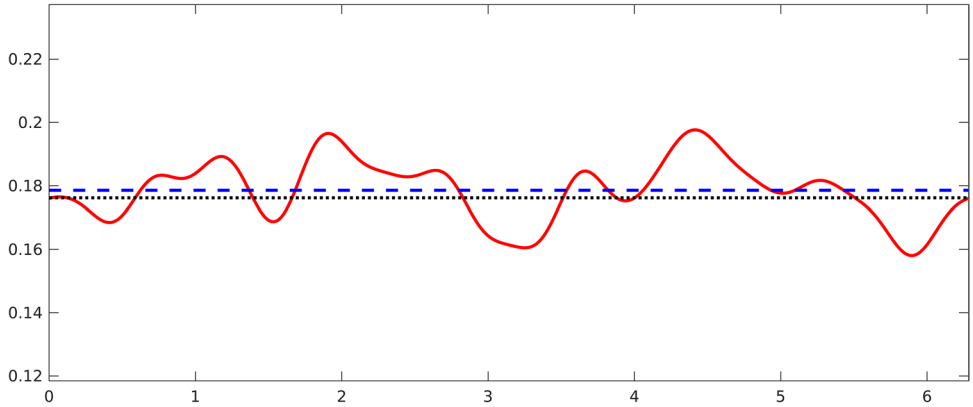

Figure 5. Reconstructed wall shear stress $\tau^{\delta,\epsilon}_{\alpha,\beta}$ (solid red) and constant approximation $\overline{\tau}^{\delta,\epsilon}_{\alpha,\beta}$ (dashed blue) in comparison to the reference wall shear stress τ^{ref} (dotted black) obtained by simulation. All results are functions of angle φ with values in Pa.

flow simulation [12]. Note that the average wall shear stress $\overline{\tau}^{\delta,\epsilon}_{\alpha,\beta}$ is in very good agreement with the reference value τ^{ref} obtained for the simulated data. The local variations in the reconstruction $\tau^{\delta,\epsilon}_{\alpha,\beta}$ can be explained by the turbulent variations of velocity in the data; also compare with the plots in figures 3 and 4.

We now compare our wall-shear-stress estimates to those obtained by the method of Stalder [25], which is used in the flow tool of the Fraunhofer MEVIS software (www.mevis.fraunhofer.de). The basic methodology underlying this approach is the following: in a first step, a parametric approximation of the boundary of the flow geometry is determined manually from the proton density images by selecting points at the boundary and interpolation. Then, a

Table 5. Relative errors $\|\tau^* - \tau^\dagger\|_{L^2(0,2\pi)}$ in the reconstruction obtained by the method of Stalder [25] for different data resolutions.

h	1.00	0.75	0.60	0.43	0.30
$\|\tau^* - \tau^\dagger\|_{L^2(0,2\pi)}$	0.4443	0.3660	0.3078	0.3631	0.0975

smoothed velocity approximation is obtained by applying a Gaussian filter to the velocity data and cubic spline interpolation; compare with the Tikhonov filter discussed in the previous section. The estimate τ^* for the wall-shear stress can then be computed analytically. The results obtained with this approach for our data are summarized in table 5. Let us note that for most data resolutions, the errors in the estimated wall-shear stress are at least one order of magnitude larger than those obtained by our method; see table 4. Only at rather fine data resolution, the quality of the wall-shear stress estimates becomes better, which is in good agreement with the observations made by [21].

7. Discussion

As reviewed by Petersson [21], the stable and accurate estimation of wall shear stress from magnetic resonance imaging data, is a delicate issue and most reconstruction approaches reported in literature do not seem to work properly. In this paper, we therefore considered a systematic approach for the estimation of wall shear stress from magnetic resonance images of proton density and flow velocity, for which stability and convergence could be established under simple and realistic smoothness assumptions on the flow geometry and velocity. The theoretical results were validated by numerical tests for experimental data which demonstrate that wall shear stress can be estimated from magnetic resonance imaging data with relative errors of a few percent and practically independent of the data resolution; this is in stark contrast to the results of Stalder [25].

The presented approach can be extended to the 3D case with only minor modifications. However to obtain reasonable computation times, that are a few seconds in the 2D case and negligible compared with the preparation and acquisition time of the data, an efficient implementation is necessary.

Let us note that stable wall shear stress estimates can also be obtained via empirical Moody charts [17] or the Clauser plot method [5, 24], which are, however, limited to axisymmetric geometry or fully developed turbulent flow. Numerical simulations could also be used, in principle, to compute wall shear stress estimates [12], but precise knowledge about the rheological properties of the fluid are required. In contrast to these approaches, the method considered in this paper is generally applicable and, therefore, seems most appropriate for application in a clinical context.

Acknowledgments

Experimental data were acquired at the the University Medical Center, Freiburg, together with A Bauer (SLA, TU Darmstadt) and A Krafft, N Shokina (Med.Phys., UMC Freiburg). Funding of the authors by the German Research Foundation (DFG) via grant Eg-331/1-1 and through grant GSC 233 of the ‘Excellence Initiative’ of the German Federal and State Governments is gratefully acknowledged.

Appendix A. Geometric results

In the following, we present some auxiliary results concerning geometrical details. Recall that $D(F) = \{R \in H^2_{\text{per}}(0,2\pi) \mid r_0 < R < r_1\}$ for some $0 < r_0 < r_1 < 1$ and that $\Omega_R = \phi_R(B)$ is the image of the unit ball B under the transformation

$$\phi_R(r\cos(\varphi), r\sin(\varphi)) = (r_0 + (R(\varphi) - r_0)\, r^\eta)(\cos(\varphi), \sin(\varphi))$$

with $\eta \geqslant 2$. The Jacobian matrix of ϕ_R is denoted by J_R, and for given functions R_1, R_2, the subscripts transfer to the associated objects, e.g. $\phi_1 = \phi_{R_1}$ and $J_2 = J_{R_2}$.

As a first result, we estimate the differences of domains $\Omega_R = \phi_R(B)$ in terms of differences of their parameterizing radius functions.

Lemma A.1. *Let $R_1, R_2 \in D(F)$. Then*

$$|\Omega_1 \setminus \Omega_2| \leqslant C\|R_1 - R_2\|_{H^1(0,2\pi)}. \tag{A.1}$$

Proof. Let us define $R_{\max}(\varphi) = \max\{R_1(\varphi), R_2(\varphi)\}$. Then

$$\begin{aligned}|\Omega_1 \setminus \Omega_2| = \int_0^{2\pi} \int_{R_2(\varphi)}^{R_{\max}(\varphi)} r\,\mathrm{d}r\,\mathrm{d}\varphi &= \frac{1}{2}\int_0^{2\pi} (R_{\max}(\varphi) + R_2(\varphi))(R_{\max}(\varphi) - R_2(\varphi))\,\mathrm{d}\varphi \\ &\leqslant 2\pi r_1 \|R_{\max} - R_2\|_{L^\infty(0,2\pi)} \leqslant 2\pi r_1 C\|R_1 - R_2\|_{H^1(0,2\pi)}.\end{aligned}$$

In the last step, we used the continuous embedding $H^1(0,2\pi) \hookrightarrow L^\infty(0,2\pi)$. □

As a next step, we estimate differences in the normal vector n_R defined in (20), in terms of differences in the radius function.

Lemma A.2. *Let $R_1, R_2 \in D(F)$. Then*

$$\|n_1 - n_2\|_{L^\infty(\partial B)} \leqslant C\,\|R_1 - R_2\|_{H^2(0,2\pi)}. \tag{A.2}$$

Proof. Let us introduce $e_r = (\cos(\varphi), \sin(\varphi))$ and $e_\varphi = (-\sin(\varphi), \cos(\varphi))$. Omitting the explicit notion of the dependence on φ, we then obtain for any angle φ that

$$|n_1 - n_2|^2 = |\lambda_r\, e_r + \lambda_\varphi\, e_\varphi|^2 = \lambda_r^2 + \lambda_\varphi^2.$$

The radial component of the difference can be estimated by

$$\begin{aligned}|\lambda_r| &= \left|\frac{R_1}{\sqrt{R_1^2 + R_1'^2}} - \frac{R_2}{\sqrt{R_2^2 + R_2'^2}}\right| \leqslant \left|\frac{R_1 - R_2}{\sqrt{R_1^2 + R_1'^2}} + R_2\frac{\sqrt{R_2^2 + R_2'^2} - \sqrt{R_1^2 + R_1'^2}}{\sqrt{R_1^2 + R_1'^2}\sqrt{R_2^2 + R_2'^2}}\right| \\ &\leqslant \frac{|R_1 - R_2|}{r_0} + R_2\frac{\sqrt{(R_1 - R_2)^2 + (R_1' - R_2')^2}}{\sqrt{R_1^2 + R_1'^2}\sqrt{R_2^2 + R_2'^2}} \leqslant \frac{1+\sqrt{2}}{r_0}\|R_1 - R_2\|_{W^{1,\infty}(0,2\pi)}.\end{aligned}$$

In a similar way, one can estimate λ_φ, and by Sobolev's embedding theorem, we obtain

$$\|n_1 - n_2\|_{L^\infty(\partial B)} \leqslant \|\lambda_r\|_{L^\infty(\partial B)} + \|\lambda_\varphi\|_{L^\infty(\partial B)} \leqslant C\|R_1 - R_2\|_{H^2(0,2\pi)},$$

which already yields the desired estimate. □

The following result ensures smoothness of the transformations ϕ_R whenever the radius function R is sufficiently smooth.

Lemma A.3. *Let $R_1, R_2 \in D(F) \cap H^k_{\text{per}}(0,2\pi)$ for $k \leqslant \eta$ with $\eta \geqslant 2$ as in (10). Then*

$$\|\phi_1\|_{W^{k-1,\infty}(B)} \leqslant C\|R_1\|_{H^k(0,2\pi)} \tag{A.3}$$

where $\phi_1 = \phi_{R_1}$ with ϕ_R defined in (10). Moreover,

$$\|\phi_1 - \phi_2\|_{W^{k-1,\infty}(B)} \leqslant C\|R_1 - R_2\|_{H^k(0,2\pi)}. \tag{A.4}$$

Proof. The continuity of ϕ_1 is obvious and the Jacobian $J_1 = J_{R_1}$ obtained by derivation with respect to coordinates $x = (r\cos\phi, r\sin\phi)$ reads

$$J_1(r\cos\varphi, r\sin\varphi) = \begin{pmatrix} r_0 + \eta\,(R_1(\varphi) - r_0)\,r^{\eta-1} & R_1'(\varphi)\,r^{\eta-1} \\ 0 & r_0 + (R_1(\varphi) - r_0)\,r^{\eta-1} \end{pmatrix}. \tag{A.5}$$

Since $\eta \geqslant 2$, the Jacobian can be seen to be continuous also in $r = 0$, and we have

$$\|J_1\|_{L^\infty(B)} \leqslant C\,(\|R_1\|_{L^\infty(0,2\pi)} + \|R_1'\|_{L^\infty(0,2\pi)}) \leqslant C\|R_1\|_{H^2(0,2\pi)}.$$

This shows the first estimate for $k = 1$. The assertion for higher order derivatives of ϕ_1 follow in a similar way. From the formula (10), one can see that ϕ_R is affine linear in R. Hence the second estimate follows directly from the first. □

As a next step, we show that the transformations ϕ_R defined in (10) are invertible.

Lemma A.4. *Let $R \in D(F)$. Then the transformation ϕ_R defined in (10) is a diffeomorphism with inverse transformation $\psi_R = (\phi_R)^{-1}$ and*

$$\|J_R^{-1}\|_{L^\infty(B)} = \|J_{\psi_R}\|_{L^\infty(\Omega_R)} \leqslant C\,\|R\|_{H^2(0,2\pi)}. \tag{A.6}$$

Proof. Using (A.5), we can estimate the determinant by

$$\det(J_R(r\cos\varphi, r\sin\varphi)) = (r_0 + \eta(R(\varphi) - r_0)r^{\eta-1}) \cdot (r_0 + (R(\varphi) - r_0)r^{\eta-1}) \geqslant r_0^2.$$

The existence of an inverse transformation $\psi_R = (\phi_R)^{-1}$ then follows form the implicit function theorem and the Jacobian of the inverse mapping is $J_{\psi_R} \circ \phi_R = J_R^{-1}$. The bounds for J_{ψ_R} can then be deduced in an elementary way. □

Using the previous results, we can also bound differences in the inverse mappings.

Lemma A.5. *Let $R_1, R_2 \in D(F)$ and assume that $R_1 \in H^3_{\text{per}}(0,2\pi)$. Furthermore, let ψ_1, ψ_2 denote the corresponding inverse transformations with Jacobians J_{ψ_1}, J_{ψ_2}. Then*

$$\|\psi_1 - \psi_2\|_{L^\infty(\Omega_1\cap\Omega_2)} \leqslant C\,\|R_1 - R_2\|_{H^1(0,2\pi)} \tag{A.7}$$

and the difference in the Jacobians can be bounded by

$$\|J_{\psi_1} - J_{\psi_2}\|_{L^\infty(\Omega_1\cap\Omega_2)} \leqslant C\,\|R_1 - R_2\|_{H^2(0,2\pi)}. \tag{A.8}$$

Proof. *Step 1:* To show (A.7), let $x \in \Omega_1 \cap \Omega_2$. Then there are $x_1, x_2 \in B$ with $\phi_1(x_1) = \phi_2(x_2) = x$. Since the transformations ϕ_1 and ϕ_2 preserve angles, the angular parts $\varphi(x_1) = \varphi(x_2) = \varphi(x) =: \varphi$ are equal. ϕ_2 has an inverse ψ_2, hence

$$x_2 - x_1 = \psi_2(\phi_2(x_2)) - \psi_2(\phi_2(x_1)) = \psi_2(x) - \psi_2(x + \mathrm{d}x),$$

where the defect is given by

$$\mathrm{d}x = \phi_2(x_1) - \phi_1(x_1) = (R_2(\varphi) - R_1(\varphi))|x_1|^\eta(\cos(\varphi), \sin(\varphi)).$$

Since x and $\mathrm{d}x$ have the same angular coordinate and Ω_2 is star shaped with respect to the origin, we have $\{x + t\mathrm{d}x | t \in [0,1]\} \subset \Omega_2$. The mean value theorem yields

$$|\psi_2(x) - \psi_1(x)| = |x_2 - x_1| = |J_{\psi_2}(\xi)\mathrm{d}x| \leqslant \|J_{\psi_2}\|_{W^{1,\infty}(\Omega_2)} \|R_1 - R_2\|_{H^1(0,2\pi)}.$$

The assertion (A.7) follows by the estimate of lemma A.4 *Step 2: Show (A.8).* Starting at (A.5) elementary calculus yields

$$\|\det J_{\phi_1} - \det J_{\phi_2}\|_{L^\infty(B)} \leqslant C \|R_1 - R_2\|_{L^\infty(0,2\pi)},$$

where the constant C depends only on $\|R_1\|_{L^\infty(0,2\pi)}$, $\|R_2\|_{L^\infty(0,2\pi)}$, r_0 and η. For the inverse Jacobians, we further conclude that

$$\begin{aligned}
\|J_{\phi_1}^{-1} - J_{\phi_2}^{-1}\|_{L^\infty(B)} &\leqslant \left\| \frac{1}{\det J_{\phi_1}} J_{\phi_1} - \frac{1}{\det J_{\phi_2}} J_{\phi_2} \right\|_{L^\infty(B)} \\
&\leqslant \left\| \frac{\det J_{\phi_2} - \det J_{\phi_1}}{\det J_{\phi_1} \det J_{\phi_2}} J_{\phi_1} \right\|_{L^\infty(B)} + \left\| \frac{1}{\det J_{\phi_2}} (J_{\phi_1} - J_{\phi_2}) \right\|_{L^\infty(B)} \\
&\leqslant C \left(\frac{1}{r_0^4} \|R_1\|_{H^2(0,2\pi)} + \frac{1}{r_0^2} \right) \|R_1 - R_2\|_{H^2(0,2\pi)}.
\end{aligned}$$

Since the inverse Jacobian of ϕ_1 has the representation $J_{\phi_1}^{-1} = \tilde{J}_{\phi_1} / \det J_{\phi_1}$, where $\tilde{J}_{\phi_1}$ is a rearrangement of J_{ϕ_1} and all expressions are continuously differentiable, one can verify without difficulty that $J_{\phi_1}^{-1} \in W^{1,\infty}(B)$ with the associated norm bounded in terms of η, r_0, and $\|R_1\|_{H^3(0,2\pi)}$. Therefore we arrive at (A.8) by

$$\begin{aligned}
\|J_{\psi_1} - J_{\psi_2}\|_{L^\infty(\Omega_1 \cap \Omega_2)} &= \|J_{\phi_1}^{-1} \circ \psi_1 - J_{\phi_2}^{-1} \circ \psi_2\|_{L^\infty(\Omega_1 \cap \Omega_2)} \\
&\leqslant \|J_{\phi_1}^{-1}\|_{W^{1,\infty}(B)} \|\psi_1 - \psi_2\|_{L^\infty(\Omega_1 \cap \Omega_2)} + \|J_{\phi_1}^{-1} - J_{\phi_2}^{-1}\|_{L^\infty(B)} \\
&\leqslant C \|R_1 - R_2\|_{H^2(0,2\pi)}.
\end{aligned}$$

This completes the proof of the second estimate of the lemma. □

Appendix B. Interpretation of the data

Let us briefly comment on the physical interpretation and the preprocessing of the experimental data used for the reconstructions in section 6.

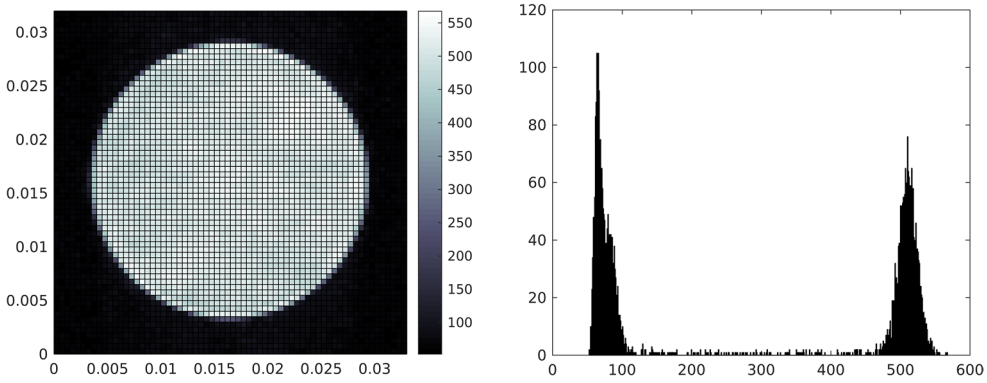

Figure B1. Magnitude raw data (left) and magnitude value histogram (right) used to normalize the magnitude data.

B.1. Magnitude data

The magnitude raw data m^δ_{raw} represent integral means of the proton density over voxels; these values are additionally perturbed by data noise. From a histogram of the magnitude data, see figure B1, one can deduce to peak values m_0 and m_1, which are used for scaling of the data.

Based on the two values m_0, m_1, the normalized magnitude m^δ are then defined by

$$m^\delta|_{V_i} = T\left(\frac{m^\delta_{\text{raw}}|_{V_i} - m_0}{m_1 - m_0}\right),$$

with truncation function $T(x) = \max(0, \min(1, x))$. These measurements then represent an approximation for the characteristic function of the flow domain.

B.2. Velocity data

The raw data acquired in phase contrast magnetic resonance velocimetry can be interpreted as

$$d^\delta|_{V_i} = \int_{V_i} \rho(x) \mathrm{e}^{\mathrm{i}2\pi u(x)/v_{\text{enc}}} + \text{noise},$$

where ρ is the proton density and v_{enc} the velocity encoding parameter. An average value of the velocity in the voxel V_i is then recovered as the phase of this signal, i.e.

$$u^\delta|_{V_i} = v_{\text{enc}} \cdot \arg(d^\delta|_{V_i}). \tag{B.1}$$

Phase unwrapping may be required, if the maximal velocity is larger then v_{enc}. In the absence of data noise and assuming that the proton density is given by $\rho = c\chi_\Omega$, one can use Taylor approximation to deduce that

$$u^\delta|_{V_i} \approx \frac{1}{|V_i \cap \Omega|} \int_{V_i \cap \Omega} u(x)\mathrm{d}x,$$

where Ω is the flow domain and u the true flow velocity. This is the measurement model used in the numerical tests. Let us note that the phase retrieval in (B.1) is particularly sensitive to data perturbations, if $\mathrm{abs}(d^\delta|_{V_i})$ is small, which is the case close to the boundary and outside the flow domain. Therefore, particularly large noise in the velocity data is expected for these voxels; compare with figure 3.

ORCID iDs

H Egger https://orcid.org/0000-0003-3769-8791

References

[1] Bauer A, Wegt S, Tropea C, Krafft A, Shokina N, Hennig J, Teschner G and Egger H 2018 Ground-truth for measuring wall shear stress with magnetic resonance velocimetry *19th Int. Symp. on the Application of Laser and Imaging Techniques to Fluid Mechanics*
[2] Canny J 1986 A computational approach to edge detection *IEEE Trans. Pattern Anal. Mach. Intell.* **6** 679–98
[3] Cheng C, Parker D and Taylor C A 2002 Quantification of wall shear stress in large blood vessels using Lagrangian interpolation functions with CINE phase-contrast magnetic resonance imaging *Ann. Biomed. Eng.* **30** 1020–32
[4] Cheng C, Tempel D, van Haperen R, van der Baan A, Grosveld F, Daemen M J, Krams R and de Crom R 2006 Atherosclerotic lesion size and vulnerability are determined by patterns of fluid shear stress *Circulation* **113** 2744–53
[5] Clauser F H 1956 The turbulent boundary layer *Adv. Appl. Mech.* **4** 1–51
[6] Egger H and Hofmann B 2018 Tikhonov regularization in Hilbert scales under conditional stability assumptions *Inverse Problems* **34** 115015
[7] Egger H and Leitão A 2009 Nonlinear regularization methods for ill-posed problems with piecewise constant or strongly varying solutions *Inverse Problems* **25** 115014
[8] Engl H W, Hanke M and Neubauer A 1996 *Regularization of Inverse Problems* (*Mathematics and its Applications* vol 375) (Dordrecht: Kluwer)
[9] Gilbarg D and Trudinger N S 2001 *Elliptic Partial Differential Equations of Second Order* (*Grundlehren der Mathematischen Wissenschaften* vol 224) (Berlin: Springer)
[10] Gimbrone M A, Nagel T and Topper J N 1997 Biomechanical activation: an emerging paradigm in endothelial adhesion biology *J. Clin. Invest.* **99** 1809–13
[11] Kaltenbacher B, Neubauer A and Scherzer O 2008 *Iterative Regularization Methods for Nonlinear Ill-Posed Problems* (*Radon Series on Computational and Applied Mathematics* vol 6) (Berlin: de Gruyter & Co)
[12] Khoury G K E, Schlatter P, Noorani A, Fischer P F, Brethouwer G and Johansson A V 2013 Direct numerical simulation of turbulent pipe flow at moderately high Reynolds numbers *J. Flow Turbul. Combust.* **91** 475–95
[13] Lunardi A 2009 *Interpolation Theory* (Pisa: Edizione della Normale)
[14] Margotti F, Rieder A and Leitão A 2014 A Kaczmarz version of the `reginn`-Landweber iteration for ill-posed problems in Banach spaces *SIAM J. Numer. Anal.* **52** 1439–65
[15] Markl M, Frydrychowicz A, Kozerke S, Hope M and Wieben O 2012 4D flow MRI *J. Magn. Reson. Imaging* **36** 1015–36
[16] Modersitzki J 2004 *Numerical Methods for Image Registration* (New York: Oxford University Press)
[17] Moody L F 1944 Friction factors for pipe flow *Trans. ASME* **66** 671–84
[18] Neubauer A 1988 When do Sobolev spaces form a Hilbert scale? *Proc. Am. Math. Soc.* 103 557–62
[19] Niebauer J and Gooke J P 1996 Cardiovascular effects of exercise: role of endothelial shear stress *J. Am. Coll. Cardiol.* **28** 1652–60
[20] Oyre S, Ringgaard S, Kozerke S, Paaske W P, Scheidegger M B, Boesiger P and Pedersen E M 1998 Quantitation of circumferential subpixel vessel wall position and wall shear stress by multiple sectored three-dimensional paraboloid modeling of velocity encoded Cine MR *Magn. Reson. Med.* **40** 645–55
[21] Petersson S, Dyverfeldt P and Ebbers T 2012 Assessment of the accuracy of MRI wall shear stress estimation using numerical simulations *Magn. Reson. Imaging* **36** 128–38
[22] Potters W V, Ooij P, Marquering H, van Bavel E and Nederveen A J 2015 Volumetric arterial wall shear stress calculation based on cine phase contrast MRI *J. Magn. Reson. Imaging* **41** 505–16
[23] Shojima M, Oshima M, Takagi K, Torii R, Hayakawa M, Katada K, Morita A and Kirino T 2004 Magnitude and role of wall shear stress on cerebral aneurysm: computational fluid dynamic study of 20 middle cerebral artery aneurysms *Stroke* **35** 2500–5

[24] Shokina N, Buchenberg W B, Menza M, Bauer A, Teschner G, Tropea C, Egger H, Hennig J and Krafft A J 2018 Accurate MR-based wall shear stress measurements in fully developed turbulent flow using the Clauser-plot method *Abstract No 2946 in Joint Annual Meeting ISMRM-ESMRMB (Paris, France, 16–21 June 2018)*

[25] Stalder A F, Russe M F, Frydrychowicz A, Bock J, Hennig J and Markl M 2008 Quantitative 2D and 3D phase contrast MRI: optimized analysis of blood flow and vessel wall parameters *Magn. Reson. Imaging* **60** 1218–31

[26] Tang C, Blatter D D and Parker D L 1993 Accuracy of phase-contrast flow measurements in the presence of partial-volume effects *J. Magn. Reson. Imaging* **3** 377–85

[27] Tautenhahn U 1998 On a general regularization scheme for nonlinear ill-posed problems. II. Regularization in Hilbert scales *Inverse Problems* **14** 1607–16

[28] Tikhonov A N and Arsenin V Y 1977 *Solutions of Ill-Posed Problems* (*Scripta Series in Mathematics*) (Washington, DC: John Wiley & Sons)